AGU PUBLICATIONS

JGR

Journal of Geophysical Research: Space Physics

RESEARCH ARTICLE
10.1002/2017JA025019

Special Section:
Magnetospheric Multiscale (MMS) Mission Results Throughout the First Primary Mission Phase

MMS Observation of Asymmetric Reconnection Supported by 3-D Electron Pressure Divergence

K. J. Genestreti[1], A. Varsani[1], J. L. Burch[2], P. A. Cassak[3], R. B. Torbert[2,4], R. Nakamura[1], R. E. Ergun[5,6], T.-D. Phan[7], S. Toledo-Redondo[8], M. Hesse[9], S. Wang[10], B. L. Giles[11], C. T. Russell[12], Z. Vörös[1], K.-J. Hwang[2], J. P. Eastwood[13], B. Lavraud[14], C. P. Escoubet[15], R. C. Fear[16], Y. Khotyaintsev[17], T. K. M. Nakamura[1], J. M. Webster[18], and W. Baumjohann[1]

[1]Space Research Institute, Austrian Academy of Sciences, Graz, Austria, [2]Southwest Research Institute, San Antonio, TX, USA, [3]Department of Physics and Astronomy, West Virginia University, Morgantown, WV, USA, [4]Space Science Center, University of New Hampshire, Durham, NH, USA, [5]Department of Astrophysical and Planetary Sciences, University of Colorado Boulder, Boulder, CO, USA, [6]Laboratory for Atmospheric and Space Physics, University of Colorado Boulder, Boulder, CO, USA, [7]Space Science Institute, University of California Berkeley, Berkeley, CA, USA, [8]Science Directorate, European Space Agency, ESAC, Madrid, Spain, [9]Birkeland Centre for Space Science, University of Bergen, Bergen, Norway, [10]Astronomy Department, University of Maryland, College Park, MD, USA, [11]Heliophysics Science Division, NASA Goddard Space Flight Center, Greenbelt, MD, USA, [12]Institute of Geophysics and Planetary Physics, University of California, Los Angeles, CA, USA, [13]The Blackett Laboratory, Imperial College London, London, UK, [14]Institute de Recherche en Astrophysique et Planétologie, Toulouse, France, [15]Space Science Department, European Space Agency, Noordwijk, Netherlands, [16]Department of Physics & Astronomy, University of Southampton, Southampton, UK, [17]Swedish Institute of Space Physics, Uppsala, Sweden, [18]Department of Physics and Astronomy, Rice University, Houston, TX, USA

Key Points:
- We analyze MMS data measured during a slow crossing of the density-asymmetric magnetopause
- Ion and electron dynamics are consistent with a normal crossing of an inner diffusion region
- $\vec{J} \cdot \vec{E}'$ appeared to result from in and out-of-plane gradients of gyrotropic and agyrotropic electron pressure tensor

Correspondence to:
K. J. Genestreti,
kevin.genestreti@oeaw.ac.at

Citation:
Genestreti, K. J., Varsani, A., Burch, J. L., Cassak, P. A., Torbert, R. B., Nakamura, R., et al. (2018). MMS observation of asymmetric reconnection supported by 3-D electron pressure divergence. *Journal of Geophysical Research: Space Physics*, *123*, 1806–1821. https://doi.org/10.1002/2017JA025019

Received 17 NOV 2017
Accepted 5 FEB 2018
Accepted article online 8 FEB 2018
Published online 6 MAR 2018

Abstract We identify the electron diffusion region (EDR) of a guide field dayside reconnection site encountered by the Magnetospheric Multiscale (MMS) mission and estimate the terms in generalized Ohm's law that controlled energy conversion near the X-point. MMS crossed the moderate-shear (~130°) magnetopause southward of the exact X-point. MMS likely entered the magnetopause far from the X-point, outside the EDR, as the size of the reconnection layer was less than but comparable to the magnetosheath proton gyroradius, and also as anisotropic gyrotropic "outflow" crescent electron distributions were observed. MMS then approached the X-point, where all four spacecraft simultaneously observed signatures of the EDR, for example, an intense out-of-plane electron current, moderate electron agyrotropy, intense electron anisotropy, nonideal electric fields, and nonideal energy conversion. We find that the electric field associated with the nonideal energy conversion is (a) well described by the sum of the electron inertial and pressure divergence terms in generalized Ohms law though (b) the pressure divergence term dominates the inertial term by roughly a factor of 5:1, (c) both the gyrotropic and agyrotropic pressure forces contribute to energy conversion at the X-point, and (d) both out-of-the-reconnection-plane gradients ($\partial/\partial M$) and in-plane ($\partial/\partial L, N$) in the pressure tensor contribute to energy conversion near the X-point. This indicates that this EDR had some electron-scale structure in the out-of-plane direction during the time when (and at the location where) the reconnection site was observed.

1. Introduction

During its magnetopause survey phase, NASA's Magnetospheric Multiscale (MMS) mission encountered a large number of plasma-kinetic-scale magnetic reconnection sites (Fuselier et al., 2017; Wang, Chen, et al., 2017). One of the key objectives of MMS is to investigate the kinetic processes that drive reconnection in the electron diffusion region (EDR) for a variety of upstream conditions (Burch et al., 2016). To this end, each magnetopause EDR observation contributes to the central goals of MMS, as it allows for events with similar and dissimilar conditions to be compared and contrasted.

1.1. Energy Conversion and Electron Dynamics During Reconnection

Burch et al. (2016) identified the role of agyrotropic "crescent-shaped" electron velocity distribution functions (eVDFs) in energy conversion in the central EDR of high-magnetic-shear reconnection, as was predicted by Hesse et al. (2014). Similarly, Burch and Phan (2016) found agyrotropic crescents in the central EDR

of moderate-shear reconnection, which was similarly predicted by Hesse et al. (2016). Khotyaintsev et al. (2016), Phan, Eastwood, et al. (2016), and Hwang et al. (2017) found that downstream of the central EDR, gyrotropic and anisotropic "outflow crescent" eVDFs can be observed. Similar to the agyrotropic crescents of Burch et al. (2016) and Hesse et al. (2014, 2016), these outflow crescents are a signature of the mixing of inflowing plasmas between the reconnection X-point and the electron stagnation point (Shay et al., 2016).

Ergun, Holmes, et al. (2016) and Ergun et al. (2017) reported observations of large-amplitude parallel electrostatic waves, which they associated with drift-instability-driven "corrugations" of the magnetopause near the separatrix and X-point. Cassak et al. (2017) and Genestreti et al. (2017) reported $\vec{J} \cdot (\vec{E} + \vec{v}_e \times \vec{B}) > 0$, the local per-volume rate of work done on the plasma by the nonideal electric field, in central EDRs that were several orders of magnitude larger than what was predicted by 2.5-d particle-in-cell (PIC) simulations. (Here the current density vector is $\vec{J}$, the electric and magnetic fields are $\vec{E}$ and $\vec{B}$, the electron bulk velocity is $\vec{v}_e$, and the electron-convective-frame electric field is defined as $\vec{E}' \equiv \vec{E} + \vec{v}_e \times \vec{B}$). While the local $\vec{J} \cdot \vec{E}'$ can be much larger than predicted, it may not be indicative of a larger-than-predicted global reconnection rate (Cassak et al., 2017).

Nakamura et al. (2017), Price et al. (2016, 2017), and Le et al. (2017) have all recently performed 3-d PIC simulations of MMS EDR events. Nakamura et al. (2017) analyzed a large-scale simulation of the very large guide field Kelvin-Helmholtz vortex reconnection event of Eriksson et al. (2016). Both the simulation and the data showed parallel out-of-plane electric fields in the $\vec{J} \cdot \vec{E}' > 0$ region that were several times larger than what is expected for the nominal fast reconnection rate of 0.1. Nakamura et al. suggested that these large-amplitude electric fields were a result of their reconnection driven by the vortex flow rather than being spontaneous. Price et al. (2017) found that small-scale turbulence developed in their simulation, causing large-amplitude parallel electric fields and structure to form in the $M - N$ plane of the current layer (see section 2 for *LMN* coordinate definition). This structured magnetopause was similar in character to the corrugated magnetopause of Ergun et al. (2017) and the lower hybrid drift turbulence of Roytershteyn et al. (2012). Price et al., 2017 noted that the wrapping of the normal electric field E_N into the direction of the current (M) resulted in greatly enhanced $\vec{J} \cdot \vec{E}'$. Le et al. (2017), which analyzed a 3-d simulation of the same event studied by Price et al. (2016, 2017), found that these oscillations in the current layer caused intense parallel electron heating as was observed by MMS (Burch et al., 2016). Price et al. noted that the turbulence caused significant anomalous resistivity in the dissipation region but did not affect the formation of the agyrotropic crescent eVDFs predicted by laminar 2.5-d PIC simulations of reconnection Hesse et al. (2014, 2016).

1.2. $\vec{J} \cdot \vec{E}'$ and Generalized Ohm's Law

Hesse et al. (2014, 2016) investigated the sources of the reconnection electric field in the central diffusion region of asymmetric reconnection with 2.5-d PIC simulations. For simulations of antiparallel and guide field ($B_M/B_L \sim 1$) reconnection, Hesse et al., 2014 determined each of the terms in generalized Ohm's law, which is

$$\vec{E}' = \eta\vec{J} - \frac{1}{en}\nabla \cdot \bar{P}_e + \frac{m_e}{en}\left(\frac{\partial \vec{J}}{e\partial t} + \nabla \cdot n\left(\vec{v}_i\vec{v}_i - \vec{v}_e\vec{v}_e\right)\right), \tag{1}$$

where e is the elementary charge, m_e is the electron mass, n is the plasma number density, $\vec{v}_i$ is the ion bulk velocity, and $\bar{P}_e$ is the electron pressure tensor (Torbert et al., 2016). Both studies found that the reconnection electric field at the X-point was balanced by the electron inertia term $-\frac{m_e}{en}\nabla \cdot n(\vec{v}_e\vec{v}_e)$ and that the reconnection electric field at the electron stagnation point was governed by the divergence of the off-diagonal (agyrotropic) elements of the electron pressure tensor. They questioned whether reconnection was then a fundamentally reversible process, given that bulk inertial effects appeared to dominate at the reconnection X-point.

Torbert et al. (2016) was the first to calculate the electron inertia and pressure divergence terms of (1) with MMS data. They determined that, for the antiparallel asymmetric EDR of Burch et al. (2016), the energy conversion near the electron stagnation point was driven by both pressure divergence and electron inertia at a ratio of ~4:1. They also found that the error in the gradient approximation (and/or the anomalous resistivity) was considerable. Torbert et al., 2016 supported their findings by analyzing a 2.5-d PIC simulation of the event, which found these two terms were driving energy conversion at about the same ratio and that the anomalous resistivity term was negligible. Rager et al. (2018) analyzed the same event as Torbert et al. (2016) and found that the gradients in the perpendicular ($\sim M - L$) elements on the pressure tensor were dominant. However, they concluded that the terms in Ohm's law could not be fully accurately resolved, even with their higher time resolution (7.5 ms) electron data.

1.3. Manuscript Organization

In this study, we (1) introduce an EDR event that was observed by all four MMS spacecraft during an orbit where the tetrahedron had a very small (6.4 km) interprobe separation, (2) analyze the electron dynamics within the diffusion region, and (3) analyze the form of generalized Ohm's law near the reconnection X-point, with specific focus on the role of electron agyrotropy and 3-d (out-of-plane) structure. We find that the small interprobe separation allows us to estimate the terms in Ohm's law with greater accuracy than what has previously been reported. Furthermore, we find that the local solution to Ohm's law differs significantly from the predictions of 2.5-d PIC simulations, where $\vec{J}\cdot\vec{E}'$ may have been enhanced by turbulent, 3-d structure of the current layer. These findings are relevant to open questions about the nature of energy conversion in asymmetric EDRs, specifically regarding the influence of local fluctuations in the current sheet structure on dissipation.

The following section describes the data used in this investigation and the coordinates used to organize the data. Section 3 provides an overview of the magnetopause crossing during which the EDR was detected and an analysis of the long-duration magnetosphere-side separatrix. Section 4 analyzes the electron velocity distributions near the X-point. Section 5 analyzes the terms in generalized Ohm's law during the X-point crossing. Finally, the results are summarized, discussed, and compared/contrasted with results from a similar event in section 6.

2. Data, Analysis Methods, and LMN Coordinates

We use the highest possible resolution data from the four MMS spacecraft on 28 November 2016. Moments and VDFs for electrons are obtained by the fast plasma investigation (FPI) once per 30 ms (Pollock et al., 2016). Ion moments and VDFs are obtained by FPI once per 150 ms. Measurements of the DC magnetic field are obtained by the fluxgate magnetometers at 128 vectors per second (Russell et al., 2016). Measurements of the AC magnetic field are obtained by the search coil magnetometers at 8,196 vectors per second (Le Contel et al., 2016). The coupled AC and DC electric field vector is measured by the electric field double probes at 8,196 vectors per second (Ergun, Tucker, et al., 2016; Lindqvist et al., 2016). We use the level 2 (l2) data from the FPI, fluxgate magnetometers, and search coil magnetometer, all of which are publicly available at the MMS science data center. We use the better calibrated l3 electric field data, which are available upon request.

To calculate the pressure divergence and inertial terms in Ohm's law, we assume that within the volume of the spacecraft tetrahedron, gradients in the fields and plasma moments are approximately linear (Chanteur, 1998). A sliding overlapping boxcar scheme is used to smooth the coupled AC/DC electric field vector. When the electric field is used to calculate $\vec{J}\cdot\vec{E}'$, we use a boxcar width of 30 ms, chosen to match the cadence of FPI electron measurements.

A magnetopause-normal LMN coordinate system was determined by applying the minimization of Faraday residue (MFR) technique (Khrabrov & Sonnerup, 1998) to burst-mode magnetic and electric field data from MMS1 during a 28 s interval starting at 07:36:32 universal time (UT). Here L is the direction of maximum magnetic shear, N is the magnetopause normal, and M completes the right-handed coordinate system. In the geocentric solar ecliptic (GSE) coordinate basis, L, M, and N are [0.177617, −0.158717, 0.971216], [0.244648, −0.948804, −0.199795], and [0.953205, 0.273093, −0.129694], respectively. The average velocity of the magnetopause was −11.4 km/s $\hat{N}$, as determined with MFR. Due to the long duration of the magnetopause crossing (∼30 s), it is possible that the configuration of the magnetopause changed over the course of the event. It is also possible that kinetic-scale instabilities cause the local current and boundary orientations to differ from the larger-scale configuration (Ergun, Holmes, et al., 2016; Ergun et al., 2017; Price et al., 2016, 2017). Four-point timing analysis (Schwartz, 1998) of the B_{ZGSE} reversal point (at approximately 07:36:55 UT) yields a normal vector of [0.98011, 0.192104, −0.049797], again in GSE, and a boundary velocity of −31 km/s $\hat{N}$. These two normal vectors, one determined with MFR and the other from timing analysis, differ by approximately 10°. There is a significant difference in the two boundary velocities, as is discussed in the next section. A third boundary-normal system, local to the X-point and referred to as LMN-X, is discussed in section 4. The normal direction in LMN-X differs by less than 3° with the normal determined by MFR and by less than 7° with the normal direction from timing analysis.

3. Large-Scale Observations During the Magnetopause Crossing

On 28 November 2016 at approximately 7:36:30–7:37 UT, MMS crossed the magnetopause duskward of the subsolar point near the GSE equatorial plane (Figure 1a). The spacecraft separation was very small,

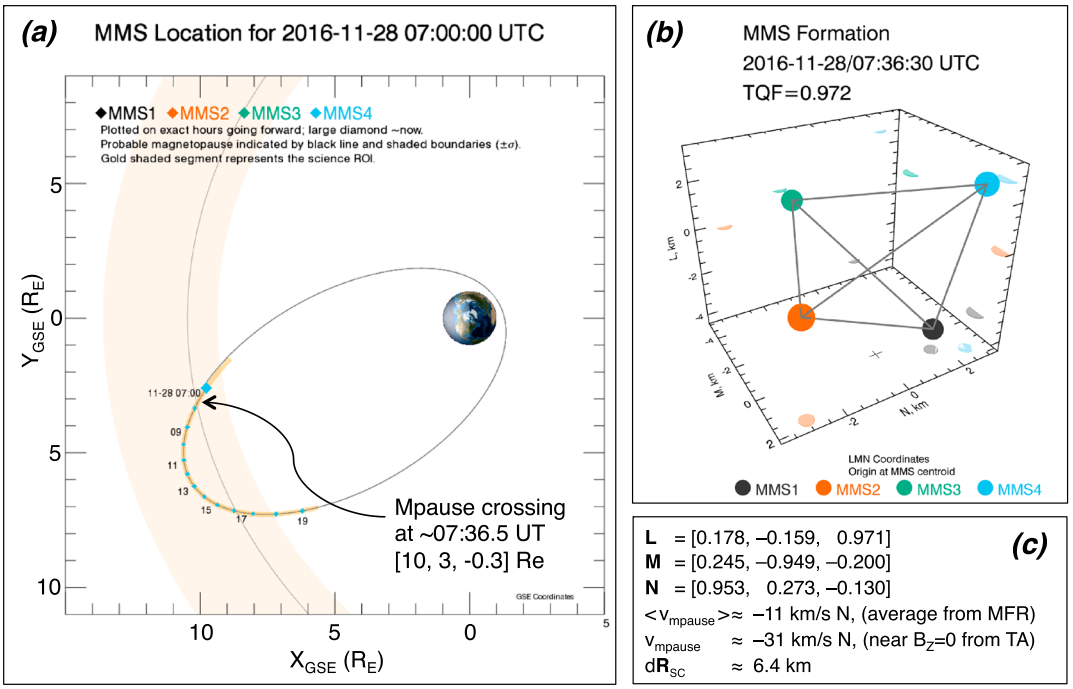

Figure 1. (a) Position of the Magnetospheric Multiscale (MMS) constellation relative to the nominal position of the magnetopause, as predicted by the empirical model of Shue et al. (1998). (b) Formation of the tetrahedron in LMN coordinates (see section 2). (c) Relevant data, including the LMN coordinate axes in geocentric solar ecliptic (GSE), the average velocity of the magnetopause determined with minimization of Faraday residue (MFR) of data from the full ~30 s crossing, the comparatively instantaneous velocity of the magnetopause determined by timing analysis of the magnetic field vector near the B_Z reversal point, and the electron inertial length d_e in the magnetosheath. Panel (a) is taken from the quicklook orbit plot archive on the MMS science data center.

with an average interprobe separation of 6.41 km ±0.50 km (Figure 1b). The crossing was directed from the magnetosphere outward into the magnetosheath and MMS obtained measurements in both inflow regions, that is, the magnetosphere proper and magnetosheath proper. The asymptotic upstream conditions are listed in Table 1, where the magnetosphere-side and magnetosheath-side parameters were determined between 7:35:10–7:36:10 UT (magnetosphere proper) and 7:37:05–7:38:05 UT (magnetosheath proper), respectively. Hereafter, the subscripts "*sh*" and "*sp*" are used to describe parameters from the magnetosheath and magnetosphere, respectively.

Table 1
Asymptotic Upstream Conditions and Parameters Related to Asymmetric Reconnection Determined from MMS1 Data

	Sphere	Sheath	Boundary parameters	
$\langle \vec{B} \rangle$ (nT)	47.65 $\hat{L}$	−20.61 $\hat{L}$	$\lvert B_{L,sh}/B_{L,sp} \rvert$	0.43
	−8.08 $\hat{M}$	−18.16 $\hat{M}$	$\lvert \langle B_M \rangle / B_{L,sh} \rvert$	0.64
	8.08 $\hat{N}$	−0.58 $\hat{N}$	Shear angle	128.6°
$\langle \lvert \vec{B} \rvert \rangle$ (nT)	49.00 ± 0.67	27.46 ± 2.81	n_{sh}/n_{sp}	26.5
$\langle \cos^{-1}(\langle \hat{b} \rangle \cdot \hat{b}) \rangle$	1.44°	7.18°	$v_{A,asym}$ [a] (km/s)	210
$\langle n \rangle$ (cm^{-3})	0.57 ± 0.17	14.99 ± 1.31	$T_{tot,asym}$ [b] (eV)	431
$\langle T_e \rangle$ (eV)	75.0 ± 19.6	42.5 ± 2.67	$v_{s,asym}$ [c] (km/s)	203
$\langle T_i \rangle$ (eV)	3711 ± 1721	333.3 ± 23.2	$d_{i,asym}$ ($d_{e,asym}$) [d] (km)	69.9 (1.63)

[a] Asymmetric Alfven speed (Cassak & Shay, 2007). [b] $T_{tot,asym}$ (Cassak et al., 2017; Shay et al., 2014). [c] Asymmetric sound speed, based on the asymmetric total temperature. [d] Asymmetric ion (electron) inertial lengths (Cassak & Shay, 2009).

Time-averaged MMS1 data from the magnetopause crossing is shown in Figure 2. The shear angle was approximately 129°. There was a strong asymmetry in B_L ($B_{L,sp}/B_{L,sh} \approx 0.4$), an average guide field approximately half the size of the magnetosheath reconnecting field ($\langle B_M \rangle / B_{L,sh} \approx 0.6$), and strong asymmetries in the temperatures ($T_{e,sh}/T_{e,sp} \approx 0.6$, $T_{i,sh}/T_{i,sp} \approx 0.09$) and density ($n_{sh}/n_{sp} \approx 27$). The positive normal B_N, which was observed throughout the crossing, and the strong negative Hall B_M, which was observed in the magnetopause plasma mixing region, both indicate that MMS crossed the magnetopause southward of an X-line. There was also a considerable asymmetry in the ion thermal pressure of $P_{i,sh}/P_{i,sp} \approx 2.3$, which was predicted to be the source of free energy for the drift instability by Price et al. (2017).

The transition from a magnetosphere-like ion population (low density with a approximately several keV component and a cold approximately hundreds eV component) to a magnetosheath-like ion population (higher density, approximately several hundred eV) began at approximately 7:36:27 UT and coincided with reversals in the L and M components of the ion bulk velocity and a reversal in the normal electric field. In Figure 2h, the reversal of E_N occurs near 7:36:26 UT and is consistent with a crossing of the magnetosphere-side separatrix given the predicted path of MMS shown in Figure 3m (Malakit et al., 2013; Shay et al., 2016). In Figure 2e, this reversal of v_{iM} occurs at the boundary between the boxes labeled "finite-gyrosphere protons" and "finite-gyrosheath protons." The second of the two $\vec{v}_i$ peaks is caused by the higher density magnetosheath protons penetrating across the magnetopause and completing half of a gyroorbit (Phan, Shay, et al., 2016), which is consistent with the observed dispersion (higher-energy larger-gyroradius sheath protons penetrate deeper into the magnetosphere, appearing in Figure 2a earlier than the lower-energy sheath protons). This explanation for the v_{iM} reversal is also consistent with the evolution of the ion distribution function between Figures 2o and 2m, where the ions are largely gyrotropic near the field reversal region (panel o) and become agyrotropic further into the magnetosphere, until eventually only sheath ions with perpendicular velocities tangential to the magnetopause are observed (panel m). The first of the two v_{iM} peaks, which had $v_{iM} > 0$, is a result of high-energy magnetospheric ions with guiding centers nearer the magnetopause being lost into the magnetosheath. A simple schematic of this effect for a 180° shear (fully antiparallel) boundary is found in Figure 2b of Phan, Shay, et al. (2016). In the case of this 28 November 2016 event, where the shear angle is less than 180°, the large v_{iL} that accompanies the large v_{iM} may result from the rotation of the Lorentz force direction in M by the moderate guide field. The strong v_{iL} is not likely associated with an ion jet, as the rotation of v_{iL} is observed before the separatrix, as discussed later in this section.

The reversal of v_{iM} is observed roughly 320 km (4.6 $d_{i,\mathrm{asym}}$) magnetosphere-ward of the B_L reversal, given a timing difference of 28 s and an average magnetopause normal velocity of −11.4 km/s, which was determined by MFR analysis (see section 2). This estimated distance is comparable to the effective ion thermal gyroradius of 305 km, based on the magnetosheath ion thermal velocity and the asymmetric ion gyrofrequency. Simulations of 2-d antiparallel reconnection predict that this finite-gyroradius effect occurs within a region roughly ±15 d_i downstream of the X-line (Shay et al., 2016), and observations of this finite-gyroradius effect have been used as evidence of close proximity to the X-point (Khotyaintsev et al., 2016; Phan, Shay, et al., 2016).

During the rotation of v_{iM}, roughly between 7:36:05–30 s UT, field-aligned streaming (upward, toward the X-point) and antifield-aligned counterstreaming (downward, away from the X-point) electrons were observed with speeds up to ~500–1,000 km/s (Figures 3a and 2f). Filamentary electron velocity enhancements have been previously identified in the MMS data (Phan, Eastwood, et al., 2016; Wang, Nakamura, et al., 2017). Figures 3e–3h show two cuts of the eVDF taken during intervals of streaming and counterstreaming low-density electrons. The upward moving electrons, in general, were observed at lower energies (~20 eV) and lower densities (~0.3 cm^{-3}), whereas the downward moving electrons were observed at higher energies (~100 eV), with slightly higher densities (~0.5 cm^{-3}) and a larger anisotropy (seen in Figure 3d and in the comparison of Figures 3f and 3h). In the 2.5-d PIC simulation of Shay et al. (2016), weak upward and strong downward parallel electron velocities were found to straddle the southern magnetosphere-side separatrix, where the magnetic field lines transition from closed to opened. In this picture, illustrated in Figure 3k, the downward moving electrons lie on reconnecting or recently reconnected field lines. Further evidence for the $\vec{v}_{e\|}$ reversal lying on or near the open-closed boundary is shown in Figure 3i, which shows that the last and strongest interval of counterstreaming electrons (near 7:36:35 UT) contained outflow crescent electrons (Hwang et al., 2017; Khotyaintsev et al., 2016; Shay et al., 2016). Anisotropic but gyrotropic "outflow" crescents, of the type shown in Figure 3i, are expected up to several d_i downstream of the center of the EDR (Shay et al., 2016).

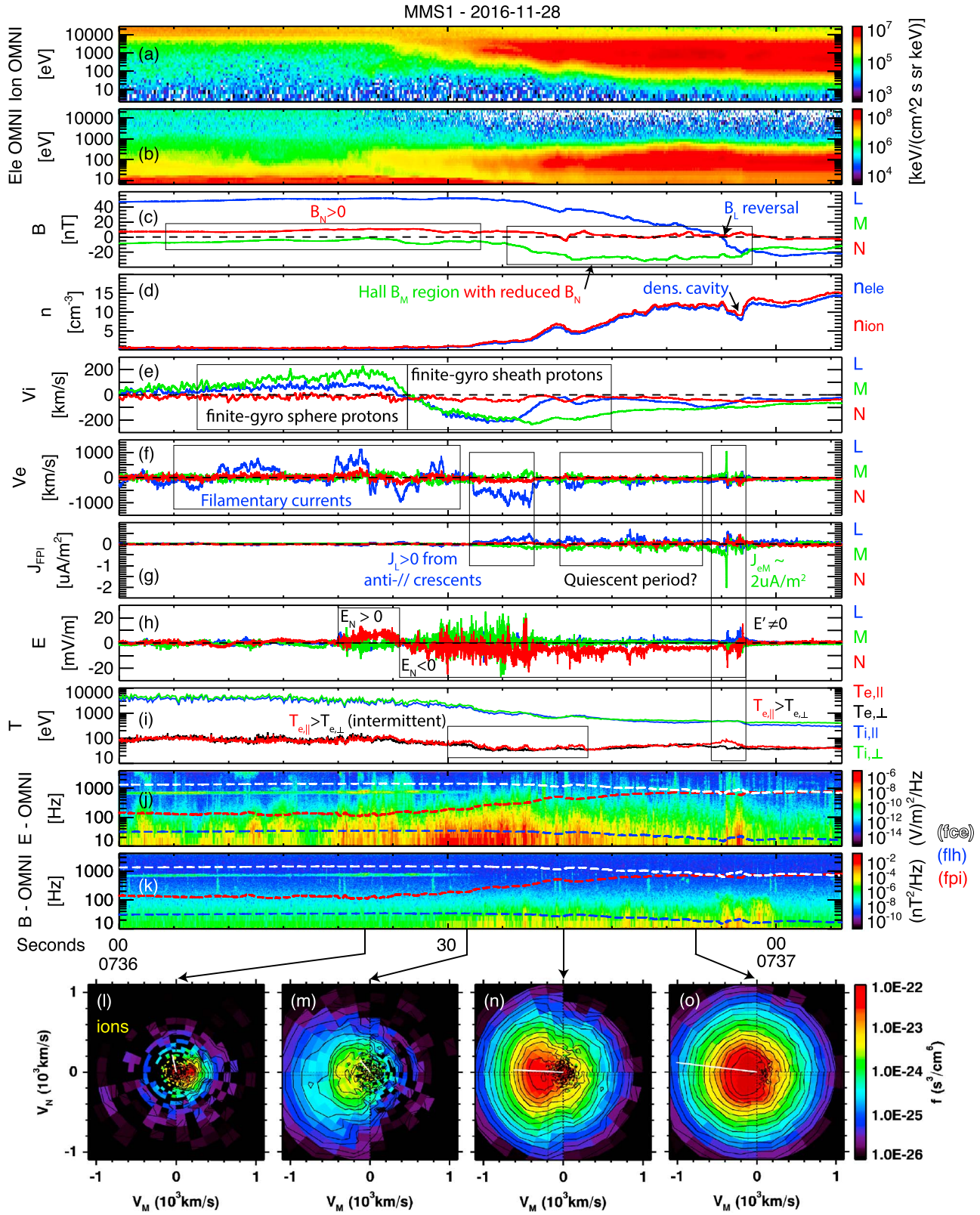

Figure 2. Omnidirectional (a) ion and (b) electron spectrograms, (c) magnetic field vector, (d) ion and electron number densities, (e) ion and (f) electron bulk velocities, (g) current density vector calculated from the plasma moments, (h) electric field vector in the spacecraft frame, (i) ion and electron temperatures, and omnidirectional (j) electric and (k) magnetic field power spectrograms. The white, blue, and red traces on panels (j) and (k) are the electron-cyclotron, lower-hybrid, and plasma-ion frequencies, respectively. (l–o) The 0.9 s averages of the ion velocity distribution function.

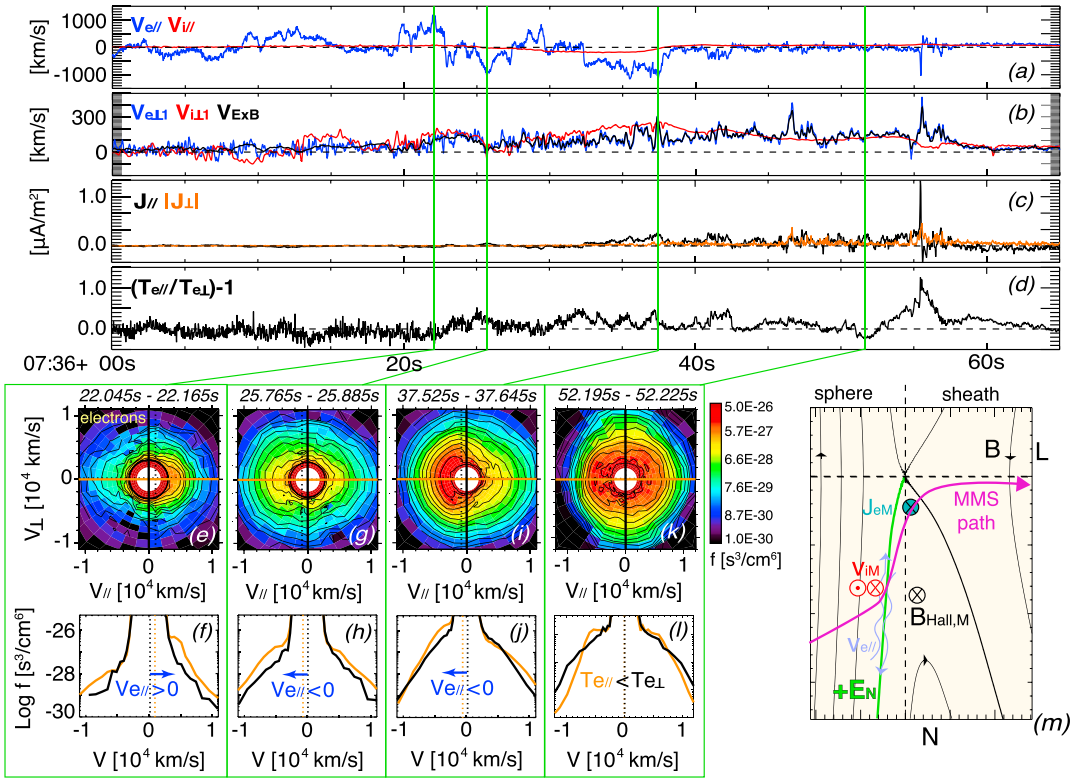

Figure 3. Plasma data from MMS1 in local (time dependent) B field coordinates. (a) Parallel and (b) perpendicular velocities of electrons (blue) and ions (red). Also in (b), the $\vec{E} \times \vec{B}$ drift velocity (black). (c) The parallel (black) and perpendicular (orange) current density. (d) The electron anisotropy. Vertical lines mark the times where (e)–(l), 2-d and 1-d cuts of electron velocity distribution functions, were measured. (m) A schematic diagram of the estimated path of Magnetospheric Multiscale (MMS) through the reconnection region with some of the observed reconnection signatures.

The multiple reversals of $\vec{v}_{e\|}$ seen in Figure 3a may indicate that MMS crossed the magnetosphere-side separatrix, returned back, then crossed again, perhaps multiple times. No similar signature of this multiple-crossing-type motion is seen in the single clean rotation of $\vec{v}_i$, which may indicate that the electron separatrix layer was moving in and out relative to the ion-scale boundary. The magnetic field data shown in Figure 2c may support this theory, as $|B_M|$ (B_L) is slightly enhanced (reduced) during the times with downward moving electrons, as would be expected for a crossing into the separatrix. Electromagnetic whistler waves with frequencies of half the electron cyclotron frequency, as are seen in Figures 2j and 2k, are predicted to form in the inflow region near the separatrix (Fujimoto, 2014). The persistence of the whistlers may indicate that MMS remained very near the separatrix for some time before finally crossing the boundary at roughly 7:36:32 UT. Waves near/below the lower-hybrid frequency are also observed throughout the separatrix crossing and also near the B_L reversal. Electrostatic waves of similar frequencies and locations have been reported in a number of EDR events and were associated with drift-instability-driven corrugations of the magnetopause current layer (Ergun, Holmes, et al., 2016; Ergun et al., 2017; Price et al., 2016, 2017). The final crossing of the separatrix occurred roughly 10 s after the reversal of v_{iM}, which implies that the thickness of the reconnection boundary layer is below the magnetosheath proton gyroscale (given that the reversal of v_{iM} is caused by penetrating sheath protons).

After the final crossing of the magnetosphere-side separatrix near 7:36:35 UT, the reconnecting magnetic field component B_L began at ~20 s and nearly monotonic decrease, excluding small fluctuations. The strength of the out-of-plane magnetic field B_M also increased substantially, as did the plasma density, whereas the normal magnetic field component B_N decreased. Between ~7:36:40–50 s UT, labeled as a "Quiescent period" in Figure 2, there are very few particle signatures that indicate proximity to an X-point (e.g., super-Alfvenic electron jets and electron crescent distributions), other than the presence of demagnetized protons (Figure 3b). We have labeled this period as "quiescent" in reference to the description by Burch and Phan (2016) of their moderate guide field EDR event, as they also found a period with little electric field activity and a reduced

temperature anisotropy between the field reversal point and the normal flow reversal point. In our quiescent period, there are no obvious *L*-directed electron jets, as have been observed between the X-point and separatrix for antiparallel reconnection events (Hwang et al., 2017). The electrons also appear magnetized during this period, with an average perpendicular bulk flow (~150 km/s) below the asymmetric Alfven speed (210 km/s, Table 1).

The quiescent period ends where the focus of the remainder of this investigation begins, at approximately 7:36:50 UT near the reversal of B_L. Many signatures of the inner diffusion region are observed in this region, including an intense and narrow out-of-plane electron current, an intense broad region of electron anisotropy with $T_{e,\|} < T_{e,\perp}$ followed by $T_{e,\|} \gg T_{e,\perp}$ (Figures 3m and 3l), and a moderate narrow region of electron agyrotropy, $\vec{J} \cdot \vec{E}' > 0$, all of which are discussed in the next section. As is shown in Figure 3c, the current near the B_L reversal is largely field aligned, which is common in MMS observations of asymmetric guide field reconnection (Burch & Phan, 2016; Chen et al., 2017; Ergun et al., 2017; Eriksson et al., 2016; Genestreti et al., 2017). It is unlikely that MMS crossed the center of the reconnection site, or the exact X-point, since the Hall field $B_M < \left\langle B_{M,\text{guide}} \right\rangle$ remained large throughout the B_L reversal interval. The magnetosheath-side separatrix was observed approximately 1.4 s after the large out-of-plane current, which, using the boundary velocity of −31 km/s $\hat{N}$ determined from timing analysis of $B_L = 0$, corresponds to a distance of 43 km (~$0.6d_{i,\text{asym}}$, where the asymmetric or hybrid inertial length d_{asym} is defined in Cassak and Shay (2009)). For comparison, the separation between the B_L reversal and the magnetosphere-side separatrix was estimated to be roughly 300 km (~4.3 $d_{i,\text{asym}}$). This asymmetry in the observed half-thickness of the reconnection layer (thicker on the magnetosphere side and thinner on the magnetosheath side) may support the path of MMS drawn in Figure 3m, where MMS entered the thicker outer diffusion region and exited the thinner inner diffusion region. After roughly 7:37 UT, following the sheath-side separatrix crossing, MMS entered and remained in the magnetosheath proper for several minutes.

In summary, we have found the following list of signatures, many of which are associated with kinetic-scale reconnection:

1. Finite-gyroradius penetration of magnetosheath protons into the magnetosphere-side inflow region, beyond the electron-scale separatrix (see reversal in v_{iM} at approximately 7:36:27 UT in Figure 2),
2. Intense parallel electron flows and antiparallel flows of "outflow" crescent electrons in the magnetosphere-side separatrix,
3. Intermittent electron anisotropy with $T_{e,\|}/T_{e,\perp}$ ~1.5 near the magnetosphere-side separatrix,
4. Electromagnetic whistler waves near the magnetosphere-side separatrix and electric field waves below f_{L-H} near the separatrix and B_L reversal,
5. A "quiescent" region with unmagnetized ions and $\vec{E}\times\vec{B}$-drifting electrons between the magnetosphere-side separatrix and the B_L reversal,
6. A reduction in B_N and drastically different distances between the two separatrices and the B_L reversal (see diagram in Figure 3m), which are consistent with an approach toward the X-point,
7. Signatures of the inner diffusion region (next section) near the B_L reversal and intense out-of-plane current (~7:36:55), and
8. Signatures of the magnetosheath-side separatrix (7:36:57) following the observation of the electron-scale J_M near the X-point and preceding entry into the magnetosheath proper.

Based on these findings, we conclude that MMS crossed the magnetosphere-side separatrix perhaps on the order of $<10-15d_i$ away from the center of the EDR. Then, MMS remained in the reconnection region while traveling northward toward the X-point, before exiting the magnetopause near the central EDR. This path is illustrated in Figure 3m.

4. Electron Dynamics Near B_L Reversal

Figure 4 shows data from the four spacecraft around the B_L reversal, where the largest out-of-plane current (Figure 4i) is observed at 7:36:55.5 UT. The vertical gray lines in Figures 4 and 5e and 5f mark the times of the eVDFs shown in Figures 5a–5d. MMS1 and 4, which crossed the current layer nearly simultaneously, both observed $J_M \approx -2$ μA/m^2 for approximately 0.15 s, which, given a boundary speed of 31 km/s, corresponds to a thickness of approximately 5 km, or 3 $d_{e,\text{asym}}$, or 0.07 $d_{i,\text{asym}}$. MMS3, which crossed after 1 and 4, and MMS2, which crossed last, both observed a J_M layer approximately half as intense and twice as thick as the current layer observed by MMS1 and 4. The average current sheet thickness was determined from the curlometer

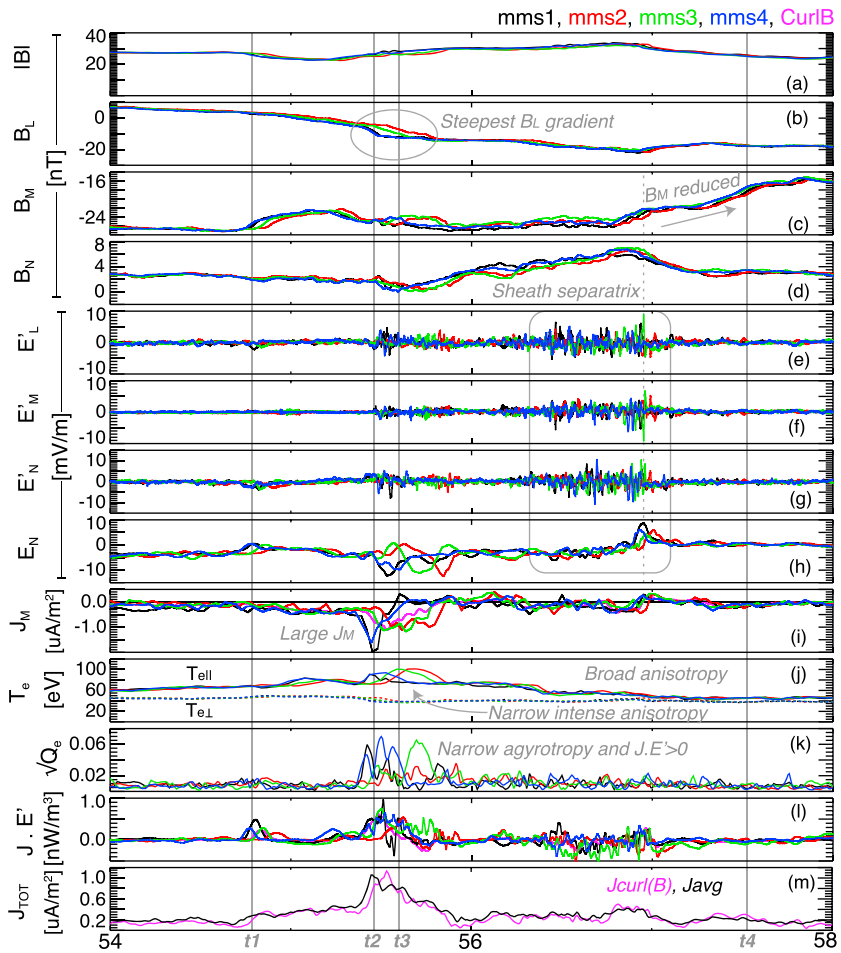

Figure 4. Data from the four spacecraft near the X-point, including (a) the total magnetic field strength, (b)–(d) the *L*, *M*, and *N* components of the magnetic field, (e)–(g) the three components of the electric field in the electron frame, (h) the normal electric field in the spacecraft frame, (i) the out-of-plane current density, (j) the electron temperatures, (k) the electron agyrotropy, (l) the electron-frame energy conversion rates, and (m) the total current density from (magenta) the curlometer method and (black) the average of the fast plasma investigation plasma moments.

current (shown in magenta in Figure 4i) to be roughly 9 km. This thickness is significantly larger than the local electron inertial length or gyroradius ($\rho_e \sim 0.6$ km, $d_e \sim 1.3$ km) and is closer to the scale suggested by Price et al. (2017) for turbulent reconnection $\sqrt{\rho_e \rho_i} \approx 13.5$ km.

The current sheet thickness is also close to the average interspacecraft separation, 6.4 km, which means that the linear gradient assumption should be applied with caution. However, since (a) the curlometer current very closely resembles the average of the currents measured by each of the four spacecraft (Figure 4m) and (b) the linear-approximate ratio of $\nabla \cdot \vec{B} / \nabla \times \vec{B}$ is small, approximately 10% at the center of the current sheet, we conclude that the linear approximation does a reasonable job of estimating the current from the curl of $\vec{B}$.

A broad temperature anisotropy of $T_{e,\parallel}/T_{e,\perp} \approx 2$ surrounds the electron J_M layer. An extreme and narrow anisotropy of $T_{e,\parallel}/T_{e,\perp} \approx 3.5$ is colocated with the J_M layer. There is also a moderate electron agyrotropy observed along with the large J_M, which, is described by the $\sqrt{Q}$ parameter of Swisdak (2016) in Figure 4k. A $\sqrt{Q}$ of 0 corresponds to a fully gyrotropic distribution, where $P_{e,\perp 1} = P_{e,\perp 2}$ and all off diagonal elements of the pressure tensor are zero. A $\sqrt{Q}$ of 1 corresponds to a fully agyrotropic distribution. For reference, the maximum value of $\sqrt{Q}$ for the 8 December 2015 guide field central magnetopause EDR event of Burch and Phan (2016) was $\sqrt{Q} = 0.09$.

During the period with the largest agyrotropy, all four MMS spacecraft also detected mostly positive $\vec{J} \cdot \vec{E}'$. The rate of energy conversion is much weaker than others have reported in the central EDR. For example,

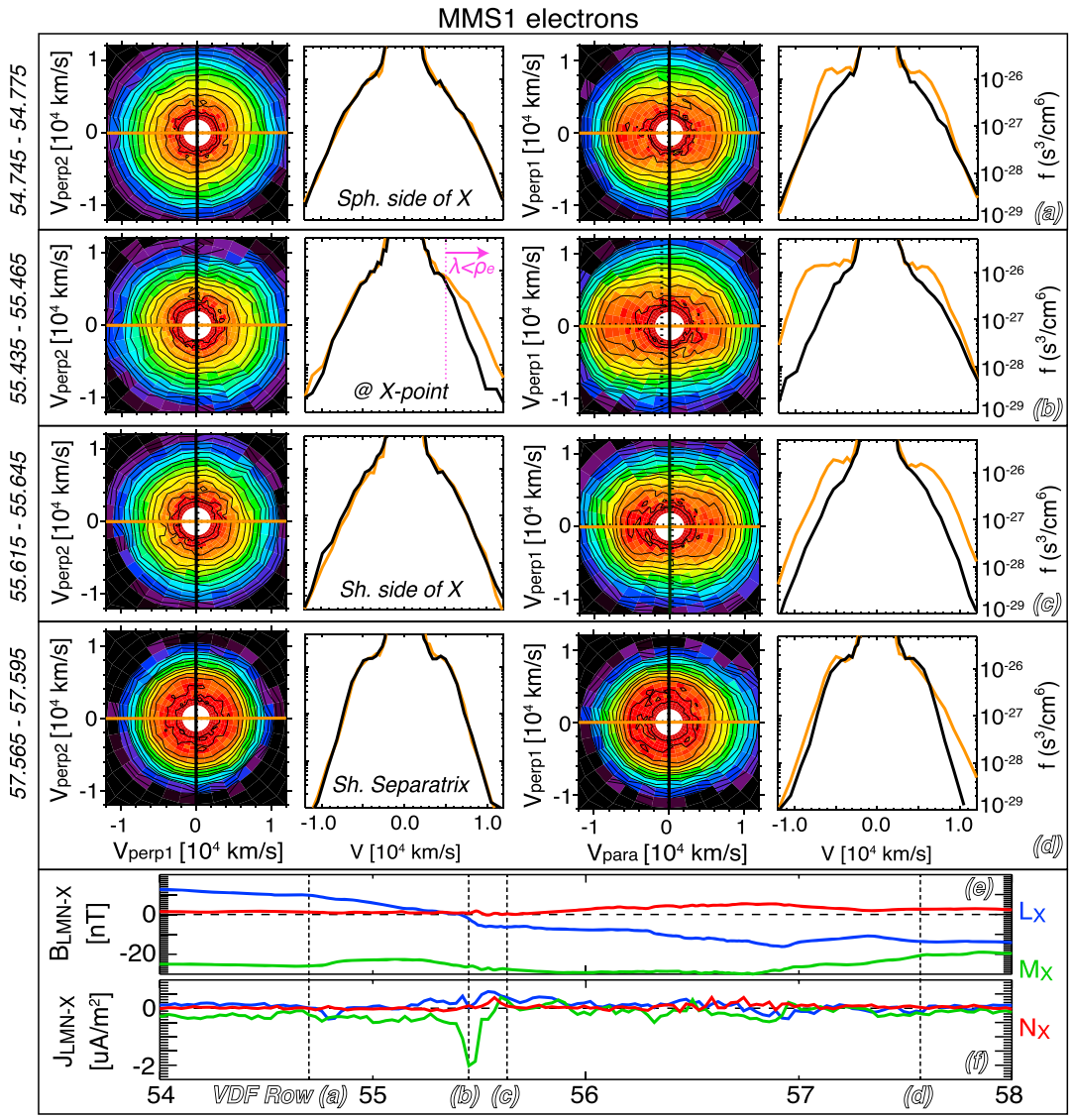

Figure 5. Data from MMS-1 near the X-point. (a)–(d) First column shows 2-d cuts of the electron velocity distribution functions (eVDF) in the $v_{\perp 1} - v_{\perp 2}$ plane, second column shows 1-d cuts along $v_{\perp 1}$ (orange) and $v_{\perp 2}$ (black), third column shows 2-d cuts in the $v_{\parallel} - v_{\perp 1}$ plane, and final column shows 1-d cuts along $v_{\parallel}$ (orange) and $v_{\perp 1}$ (black). The color bars are identical to those in Figure 3. The times where the four electron velocity distribution functions (a–d) were measured are marked on panels (e–f) with vertical lines. (e) Magnetic field and (f) current density in the LMN-X system, where $L_X = [0.157, 0.035, 0.987]$, $M_X = [0.240, -0.971, -0.0039]$, and $N_X = L_X \times M_X$.

the moderate guide field event of Burch and Phan (2016) and the nearly antiparallel event of Burch et al. (2016) had, respectively, electron-frame energy conversion rates 10 and 20 times larger than what is observed here. For antiparallel asymmetric reconnection, the largest $\vec{J} \cdot \vec{E}' > 0$ is expected near the electron stagnation point where agyrotropic electron crescent VDFs are observed. However, recent work showed that the $\vec{J} \cdot \vec{E}' > 0$ region is shifted toward the X-point for guide field asymmetric reconnection (Cassak et al., 2017; Genestreti et al., 2017).

Figure 5 shows four eVDFs from MMS1 taken near the X-point. The four rows correspond to the four times marked by solid vertical lines in Figure 4. The first two columns show that the electrons remain largely gyrotropic throughout the interval, except at the narrow region with $J_M \ll 0$ and $\vec{J} \cdot \vec{E}' > 0$ (5b). The agyrotropy is visible as an expansion (rather than a displacement) of the distribution function in the $\vec{v}_{\perp 1} > 0$ direction.

As is shown in Figure 4, the peaks of $\sqrt{Q}$, $\vec{J} \cdot \vec{E}' > 0$, and J_M are observed approximately 0.5 s after the B_L reversal. From Hesse et al. (2014, 2016), we expect that the largest electron agyrotropy should occur where

the local electron gyroradius ρ_e approaches or exceeds the local magnetic scale size $\lambda = B_L/\mu_0 J_M$, given that this is where electrons observe a considerably different B_L on either side of their orbits. Based on the data in Figure 4, this condition is only met near the B_L reversal, where the electrons are largely gyrotropic. We conclude that the LMN system determined for the entire magnetopause crossing does not organize the data near the X-point. Local LMN coordinates are therefore determined by applying minimum variance analysis to the current density vector measured by MMS1 between 52 and 59 s. In this "LMN-X" coordinate system, in which data in Figures 5e and 5f are showed, the B_{LX} reversal occurs with the peak of J_{MX} and the condition $\lambda \leq \rho_e$ is met for the period of maximum agyrotropy for electrons with energies exceeding ~80 eV. (Note that the "LMN-X" coordinates do not organize the larger-scale magnetopause crossing data as well as our previously defined LMN system).

Cuts of the eVDF within the narrow electron current layer are shown in Figure 5b. The distribution in 5b resembles adjacent eVDFs, where the phase space density in the $\vec{v}_{\parallel} < 0$ direction is significantly greater than in the $\vec{v}_{\parallel} > 0$ direction, as is consistent with the direction of the strong out-of-plane parallel current. Electrons with this type of $\vec{v}_{\parallel} - \vec{v}_{\perp}$ distribution have been observed in a very low-shear central EDR (Eriksson et al., 2016) and in a number of moderate-shear central EDRs (Genestreti et al., 2017). Genestreti et al. (2017) suggested that this type of distribution is typical of guide field X-points and that the acceleration and heating of the inflowing magnetosheath electrons along the guide field is tied to the large colocated $\vec{J} \cdot \vec{E}' > 0$. The agyrotropic $(\vec{v}_{\perp 1} - \vec{v}_{\perp 2})$ structure of the eVDF in the current layer is most pronounced for higher velocities, above roughly 5,000 km/s (80 eV), which is the same energy range for which $\lambda \leq \rho_e$.

5. Energy Conversion Near B_L Reversal

Figure 6 presents an analysis of the terms in generalized Ohm's law (equation (1)) near the B_L reversal region. For context, panels (a) and (b) show the magnetic field and current density vectors in $LMN-X$. Panel (c) shows $\vec{J} \cdot \vec{E}'$, where the measured electric field, electron velocity, and DC magnetic field vector have been used to calculate $\vec{E}'$ and the curlometer technique has been used to calculate the barycentric $\vec{J}$. Panels (d)–(e) also show the average $\vec{J} \cdot \vec{E}'$, where the electron pressure tensor divergence $\vec{E}_{\mathrm{DivPe}} = -\nabla \cdot \bar{P}_e/en$ and electron inertial $\vec{E}_{\mathrm{inertial}} = -m_e \nabla \cdot (\vec{v}_e \vec{v}_e)/en$ terms have been used to approximate $\vec{E}'$. The contribution of the ion inertial term to $\vec{J} \cdot \vec{E}'$ is negligible. We have not accounted for the terms in Ohm's law that represent time dependence of $\vec{J}$ and anomalous resistivity, which appear in equation (1). $\vec{E}_{\mathrm{DivPe}}$ and $\vec{E}_{\mathrm{inertial}}$ have been calculated with the standard 30 ms resolution electron data. We have calculated the same terms with the 7.5 ms resolution data of Rager et al. (2018), and we found no considerable differences in the form of either $\vec{E}_{\mathrm{DivPe}}$ or $\vec{E}_{\mathrm{inertial}}$, which suggests that the electron distributions were well resolved at 30 ms.

First, we compare the measured $\vec{J} \cdot \vec{E}'$ with the approximated $\vec{J} \cdot (\vec{E}_{\mathrm{DivPe}} + \vec{E}_{\mathrm{inertial}})$, given by the black curves in Figures 6c and 6d, respectively. The measured energy conversion rate peaks at ~0.8 nW/m^3 at 7:36:55.5. This positive peak is followed by a smaller negative peak of ~ −0.4 nW/m^3 at 7:36:55.7–55.8. Both the magnitude and the timing of the positive peak are approximated very well by $\vec{J} \cdot (\vec{E}_{\mathrm{DivPe}} + \vec{E}_{\mathrm{inertial}})$. The magnitude and timing of the negative peak are misestimated, being too early by 0.15 s and too large by a factor of ~2. These errors are likely a result of our approximation of generalized Ohm's law by two of four terms and/or our approximation of gradients as linear. Still, we conclude that the approximation of $\vec{J} \cdot \vec{E}' \approx \vec{J} \cdot (\vec{E}_{\mathrm{DivPe}} + \vec{E}_{\mathrm{inertial}})$ does a good job at describing the quality of the curve and a fair job at describing its quantity. The oscillations in the measured $\vec{J} \cdot \vec{E}'$, which are seen in Figure 6c between roughly 56.2 and 57 s, correspond to the region highlighted in Figures 4e–4g as the magnetosheath-side separatrix. There are no obviously correlated oscillations in our approximation of $\vec{J} \cdot \vec{E}'$ with these two terms of generalized Ohm's law.

The red and blue dashed lines in Figure 6d represent the portions of $\vec{J} \cdot \vec{E}'$ driven by electron pressure divergence and electron inertia, respectively. As is evident, the electron pressure divergence term completely dominates the energy conversion rate and nearly independently defines both the maximum and minimum of the total (black). The largest value of $\vec{J} \cdot \vec{E}_{\mathrm{inertial}}$ is ~ −0.2 nW/m^3, which, in an absolute sense, is roughly ~20% the maximum value of $\vec{J} \cdot \vec{E}_{\mathrm{DivPe}}$. The inertial electric field is also at least partially antialigned with $\vec{J}$, as is evident by the negative value of their inner product. Unlike the pressure divergence term, the largest value of $\vec{J} \cdot \vec{E}_{\mathrm{inertial}}$ is almost exactly aligned in time with the largest out-of-plane current. The largest values of both curves, though, are achieved within the out-of-plane current layer.

The black curve in Figure 6e, $\vec{J} \cdot \vec{E}_{\mathrm{DivPe}}$, is broken up into two component parts; the magenta curve represents the divergence of the gyrotropic portion of the pressure tensor, and the orange curve represents

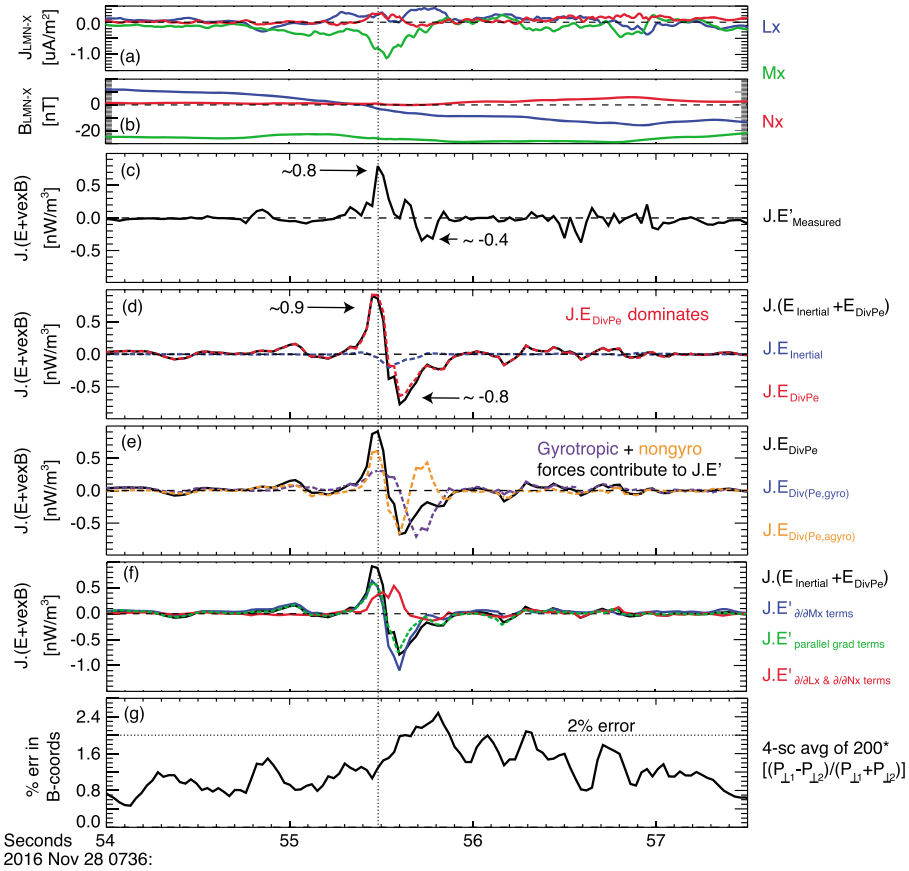

Figure 6. Analysis of generalized Ohm's law near the B_L reversal point, as shown in (a), and the intense out-of-plane electron current layer, as shown in (b). (c)–(f) The nonideal energy conversion rate determined by (c) the measured electric field and (d)–(f) the electric field approximated from the plasma electron data as $\vec{E}' \approx \vec{E}_{\mathrm{DivPe}} + \vec{E}_{\mathrm{inertial}}$. (d) A comparison of the two terms in the approximated $\vec{J} \cdot \vec{E}'$. (e) A comparison of the gyrotropic versus agyrotropic contributions to $\vec{J} \cdot (\vec{E}_{\mathrm{DivPe}} + \vec{E}_{\mathrm{inertial}})$. (f) A comparison of the in-plane versus out-of-plane gradient terms in the pressure divergence. (g) A proxy for the error in the barycentric magnetic-pressure coordinates.

the divergence of the agyrotropic portion. As is evident, both terms seem to play some role in governing the energy conversion rate near the X-point. At the exact X-point, which we have suggested to have been northward of MMS, it is expected that the agyrotropic pressure force dominates the gyrotropic force completely, whereas the opposite is expected outside the EDR (Hesse et al., 2018). In the strong positive peak of $\vec{J} \cdot \vec{E}'$, the gyrotropic term is roughly half as large as the agyrotropic term. Here both terms are positive. The story is more complicated in the negative peak of $\vec{J} \cdot \vec{E}'$, where both terms have both large positive values and large negative values in such a way that the two are partially balanced. The two terms are not fully balanced, however, and the intersection between the two curves coincides with the location of the negative peak of the overall $\vec{J} \cdot \vec{E}_{\mathrm{DivPe}}$ curve. We interpret these results, in a general sense, as an indication that MMS was located within the EDR, where agyrotropic pressure forces are nonnegligable, but outside the central EDR, where gyrotropic forces are negligible.

In order to calculate $\nabla \cdot \bar{P}_{e,\mathrm{gyro}}$ and $\nabla \cdot \bar{P}_{e,\mathrm{agyro}}$, we have organized the pressure tensor with magnetic field coordinates local to the spacecraft tetrahedron. The parallel axis is defined by the four-spacecraft-averaged field vector. The two perpendicular axes are defined such that the last two diagonal elements of the four-spacecraft-averaged pressure tensor are equivalent, that is, $\langle P_{e,\perp 1}(t) \rangle = \langle P_{e,\perp 2}(t) \rangle$, where the brackets indicate averaging over the four spacecraft and the coordinate system is time dependent. In this coordinate system, the gyrotropic elements are the diagonals and the agyrotropic elements are the off-diagonals. Invariably, given the finite separation of the four spacecraft, this coordinate system will not separate the gyrotropic and agyrotropic pressures exactly and simultaneously for all four spacecraft. By means of estimating the error in this technique, we have calculated the four-spacecraft-averaged difference between the two perpendicular

diagonal pressures, $\left\langle 2(P_{e,\perp 1} - P_{e,\perp 2})/(P_{e,\perp 1} + P_{e,\perp 2}) \right\rangle$, which is shown in Figure 6g. The average error is on the order of roughly 2% and the maximum error for a single spacecraft is less than 4% (not pictured). We interpret this as an indication that the gyrotropic and agyrotropic portions of the pressure tensor can be separated simultaneously on all four spacecraft with sufficient accuracy to warrant the qualitative interpretation offered in the previous paragraph.

Finally, we separate the divergences in $\vec{J} \cdot (\vec{E}_{\text{DivPe}} + \vec{E}_{\text{inertial}})$ by the directions of the derivatives. In Figure 6f, $\nabla_{\text{in-plane}} \cdot \bar{P}_e \equiv (\hat{L}\partial/\partial L) \cdot \bar{P}_e + (\hat{N}\partial/\partial N) \cdot \bar{P}_e$ is given by the red curve and $\nabla_{\text{out-of-plane}} \cdot \bar{P}_e \equiv (\hat{M}\partial/\partial M) \cdot \bar{P}_e$ is given by the blue curve. This separation by directional derivative is done for the combination of the much larger pressure divergence term and the much smaller inertial term. Since this sort of analysis may suffer if, for instance, N and M are not separated precisely, we complement the out-of-plane $\partial/\partial M$ term by calculating the gradients along the magnetic field direction (dashed/green curve in Figure 6f). At or very near the X-point of guide field reconnection where $B_L \approx B_N \approx 0$, the out-of-plane direction is the direction of the magnetic field, B_M. We expect this approximation to work very well near the large positive $\vec{J} \cdot \vec{E}'$ peak since it is nearest the B_L reversal, and not very well for the large negative $\vec{J} \cdot \vec{E}'$ peak as it is sheathward of the B_L reversal.

Indeed, both methods for estimating the out-of-plane gradients yield similar curves near the positive peak of $\vec{J} \cdot \vec{E}'$ and then diverge during the negative peak. We interpret this as an indication that we have separated the in and out-of-plane gradients with sufficient accuracy to claim that roughly 50% of the field-to-plasma energy conversion in this EDR was being driven by structures in the out-of-plane direction. The portion of $\vec{J} \cdot (\vec{E}_{\text{DivPe}} + \vec{E}_{\text{inertial}})$ from in-plane gradients is weak but entirely positive, which is expected in the central EDR (Shay et al., 2016; Zenitani et al., 2011), whereas the portion coming from out-of-plane gradients seems to be solely responsible for the negative energy conversion rate.

6. Conclusions

6.1. Summary

This study identified and analyzed an EDR event observed at the dayside magnetopause by Magnetospheric Multiscale (MMS) on 28 November 2016 at 7:36 UT. The magnetopause was characterized by a moderate magnetic shear angle of ~129°, a large density asymmetry of $n_{sh}/n_{sp} \approx 27$, and a large asymmetry in the reconnecting magnetic field component of $B_{L,sh}/B_{L,sp} \approx 0.4$. Additional upstream parameters are in Table 1. The EDR was observed at a time when the MMS tetrahedron was extremely small (6.4 km), which permitted the analysis of spatial gradients of the plasma moments and field data.

Finite-gyropenetrating magnetosheath protons were observed near but magnetosphere-ward of the electron separatrix, indicating that the gyroradius reconnecting layer was subion scale at the location of MMS at the start of the crossing. Similar signatures of finite-gyropenetrating magnetospheric protons were also observed, as in Phan, Shay, et al. (2016). Electron "outflow" crescents were observed within the magnetosheath-ward side of the magnetospheric separatrix, which are remote signatures of the mixing of inflowing plasmas in the central EDR between the stagnation and X-points (Hwang et al., 2017; Shay et al., 2016). Filamentary electron velocities similar to those of Phan, Eastwood, et al., (2016) and Wang, Nakamura, et al. (2017) were observed during the crossings of the magnetosphere-side separatrix. Electromagnetic whistler waves were observed prior to the final crossing, when MMS was near/in the magnetosphere-side inflow region, as predicted by Fujimoto (2014). Low-frequency electrostatic waves similar to those of Ergun, Holmes, et al. (2016) and Ergun et al. (2017) were observed at both the electron separatrix ($\pm L$-directed flow layer) and out-of-plane electron current layer. Following the crossing of the magnetospheric separatrix, a strong Hall $B_M < 0$ was observed. The Hall field remained large and negative throughout the crossing, indicating that MMS did not cross or enter the central EDR. No super-Alfvenic perpendicular electron jets were observed, despite evidence for ion demagnetization.

Near the X-point, at the reconnection site midplane, all four MMS nearly simultaneously encountered signatures of the EDR, including an intense and thin electron current layer, electron agyrotropy and anisotropy, nonideal electric fields, and nonideal energy conversion. We understood the mismatched timing of the regions where $\lambda \leq \rho_e$ and the electron agyrotropy was significant to be an indication that the LMN coordinates found for the whole crossing did not organize the data near the X-point. We then found a new LMN-X system where the inequality of Hesse et al. (2014, 2016) ($\lambda \leq \rho_e$) was satisfied during the period with the largest electron agyrotropy.

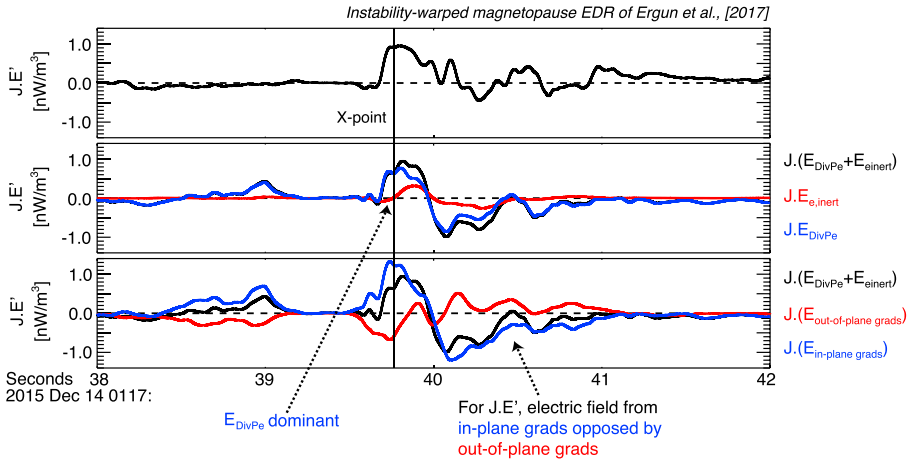

Figure 7. Analysis of generalized Ohm's law, (a) similar to Figure 6c, (b) similar to 6d, and (c) similar to 6f, but for the corrugated magnetopause event of Ergun et al. (2017).

The electrons surrounding the current layer had a roughly symmetric flat-top-type distribution in $\pm\vec{v}_{\parallel}$. The symmetry of the flat-top was broken in the electron current layer, where the distribution was significantly more extended in the antiparallel direction. The streaming of the electrons in the antiparallel direction was responsible for the current and likely related to the colocated $\vec{J}\cdot\vec{E}'>0$. The $\vec{v}_{\parallel}-\vec{v}_{\perp}$ distribution functions at the X-point were similar in character to those observed during large guide field reconnection by Eriksson et al. (2016) and during moderate guide field reconnection by Genestreti et al. (2017).

The directly measured energy conversion rate at the X-point was reasonably well approximated by $\vec{J}\cdot(\vec{E}_{\mathrm{DivPe}}+\vec{E}_{\mathrm{inertial}})$. The pressure divergence term dominated the inertial term by a wide margin. This is similar to MMS observations of the stagnation point during high-shear reconnection (Rager et al., 2018; Torbert et al., 2016) but dissimilar to the predictions of 2.5-d PIC simulations (Hesse et al., 2014, 2016). Further analysis of the pressure divergence term revealed that both the gyrotropic and agyrotropic pressure forces contributed to the overall energy conversion rate, but the meaning behind the structure and specific balance of the two terms is not currently clear. Finally, by separating the directional derivatives in the two Ohm's law terms, we found that both out-of-plane and in-plane gradients contributed to the inertial and pressure divergence terms. The portion of $\vec{J}\cdot(\vec{E}_{\mathrm{DivPe}}+\vec{E}_{\mathrm{inertial}})$ due to in-plane gradients was smaller and positive, whereas the portion from out-of-plane gradients was almost entirely responsible for the negative peak of $\vec{J}\cdot\vec{E}'$.

6.2. Discussion and Future Work

The picture of this single EDR, which was obtained by the unique capabilities of the MMS suite of plasma instruments, differs slightly from the picture of laminar and steady state 2.5-d PIC simulations. Both (a) the importance of electron agyrotropy during $\vec{J}\cdot\vec{E}'>0$ at the X-point and (b) the observation of electron outflow crescents indicate the importance of kinetic-scale mixing of inflowing plasmas in the central EDR, which is in line with previous MMS observations (Burch et al., 2016), 2.5-d PIC simulations (Hesse et al., 2014, 2016; Shay et al., 2016), and 3-d PIC simulations (Price et al., 2016, 2017). The dominance of the electron pressure divergence term differs from the predictions of 2.5-d simulations, as does the considerable contribution from out-of-plane gradients of the pressure tensor.

We suggest that the $\hat{M}(\partial/\partial M)\bar{P}_e$ term is caused by the wrapping of the $\hat{N}(\partial/\partial N)\bar{P}_e$ term into the M direction, as was predicted by Price et al. (2017). This would explain (1) the origin of the out-of-plane gradient terms and (2) why the pressure tensor divergence contributed dominantly to $\vec{J}\cdot\vec{E}'$ near our X-point, seeing as $\hat{N}(\partial/\partial N)\bar{P}_e$ is expected to be nearly an order of magnitude larger than E_M in 2.5-D simulations (Shay et al., 2016). The out-of-plane current varies significantly in the out-of-plane direction ($(J_M/d_{e,\mathrm{asym}})^{-1}\cdot\partial J_M/\partial M\sim$ 15%), which is qualitatively consistent with the picture of Price et al., 2017 More evidence is likely needed to support the relevance of this scenario to this particular event, including some analysis of the 3-d structure of the intense out-of-plane current layer observed near the B_L reversal. We have, however, found similar results for one of the corrugated magnetopause events of Ergun et al. (2017), as is shown in Figure 7. Energy conversion near the X-point is driven predominantly by the pressure divergence term, which is approximately twice

as large as the inertial term. Similar to the 28 November 2016 event, the terms resulting from out-of-plane gradients are considerable, though this time 50% as large as the in-plane gradient terms and at least partially antialigned with the current.

In the future, it would also be important to analyze 3-d simulations with similar upstream conditions to those provided in Table 1. This could be done in order to determine if $\vec{J} \cdot \vec{E}'$ and the terms in generalized Ohm's law should vary along the corrugations as $\vec{J}$ is thought to (Price et al., 2016). Finally, it is also desirable to analyze other EDR events in the same way that we have analyzed the two events in Figures 6 and 7. While we analyzed additional events from Ergun et al. (2017), none had the same clear correlation between the measured and approximated forms of $\vec{J} \cdot \vec{E}'$, which may indicate that the linear gradient assumption was invalid for these events.

Acknowledgments
The authors would like to thank everyone who contributed to the success of the MMS mission and those who contributed to the rich scientific heritage on which this mission is based. K. J. G. was funded by the FFG project 847969. R. N. was supported by Austrian Science Funds (FWF) I2016-N20. Z. V. was supported by FWF grant P28764-N27. J. P. E. was supported by the United Kingdom Science Technology Facilities Council (STFC) under grant ST/N000692/1. This event was identified during an International Space Science Institute (ISSI) meeting of the"MMS and Cluster observations of magnetic reconnection" group. K. J. G. would like to thank the EDP team, specifically Narges Ahmadi, for providing the l3 electric field data. K. J. G. would also like to thank Amy Rager, John Dorelli, and Daniel Gershman for providing us with the 7.5 ms electron data. Excepting these two data products, which are available upon request, the MMS data were obtained from the MMS Science Data Center (SDC) at the University of Colorado. The study made use of the Space Physics Environment Data Analysis Software (SPEDAS) package.

References

Burch, J. L., & Phan, T. D. (2016). Magnetic reconnection at the dayside magnetopause: Advances with MMS. *Geophysical Research Letters*, *43*, 8327–8338. https://doi.org/10.1002/2016GL069787

Burch, J. L., Moore, T. E., Torbert, R. B., & Giles, B. L. (2016). Magnetospheric multiscale overview and science objectives. *Space Science Reviews*, *199*, 5–21. https://doi.org/10.1007/s11214-015-0164-9

Burch, J. L., Torbert, R. B., Phan, T. D., Chen, L.-J., Moore, T. E., Ergun, R. E., et al. (2016). Electron-scale measurements of magnetic reconnection in space. *Science*, *352*(6290), aaf2939. https://doi.org/10.1126/science.aaf2939

Cassak, P. A., & Shay, M. A. (2007). Scaling of asymmetric magnetic reconnection: General theory and collisional simulations. *Physics of Plasmas*, *14*(10), 102114. https://doi.org/10.1063/1.2795630

Cassak, P. A., & Shay, M. A. (2009). Structure of the dissipation region in fluid simulations of asymmetric magnetic reconnection. *Physics of Plasmas*, *16*(5), 055704. https://doi.org/10.1063/1.3086867

Cassak, P. A., Genestreti, K. J., Burch, J. L., Phan, T. D., Shay, M. A., Swisdak, M., et al. (2017). The effect of a guide field on local energy conversion during asymmetric magnetic reconnection: Particle-in-cell simulations. *Journal of Geophysical Research: Space Physics*, *122*, 11,523–11,542. https://doi.org/10.1004/2017JA024555

Chanteur, G. (1998). Spatial interpolation for four spacecraft: Theory. In G. Paschmann & P. W. Daly (Eds.), *Analysis methods for multi-spacecraft data* (chap. 14, pp. 349–368). Bern, Switzerland: International Space Science Institute.

Chen, L.-J., Hesse, M., Wang, S., Gershman, D., Ergun, R. E., Burch, J., et al. (2017). Electron diffusion region during magnetopause reconnection with an intermediate guide field: Magnetospheric multiscale observations. *Journal of Geophysical Research: Space Physics*, *122*, 5235–5246. https://doi.org/10.1002/2017JA024004

Ergun, R. E., Chen, L.-J., Wilder, F. D., Ahmadi, N., Eriksson, S., Usanova, M. E., et al. (2017). Drift waves, intense parallel electric fields, and turbulence associated with asymmetric magnetic reconnection at the magnetopause. *Geophysical Research Letters*, *44*, 2978–2986. https://doi.org/10.1002/2016GL072493

Ergun, R. E., Holmes, J. C., Goodrich, K. A., Wilder, F. D., Stawarz, J. E., Eriksson, S., et al. (2016). Magnetospheric Multiscale observations of large-amplitude, parallel, electrostatic waves associated with magnetic reconnection at the magnetopause. *Geophysical Research Letters*, *43*, 5626–5634. https://doi.org/10.1002/2016GL068992

Ergun, R. E., Tucker, S., Westfall, J., Goodrich, K. A., Malaspina, D. M., Summers, D., et al. (2016). The axial double probe and fields signal processing for the MMS Mission. *Space Science Reviews*, *199*, 167–188. https://doi.org/10.1007/s11214-014-0115-x

Eriksson, S., Wilder, F. D., Ergun, R. E., Schwartz, S. J., Cassak, P. A., Burch, J. L., et al. (2016). Magnetospheric Multiscale observations of the electron diffusion region of large guide field magnetic reconnection. *Physical Review Letters*, *117*(1), 015001. https://doi.org/10.1103/PhysRevLett.117.015001

Fujimoto, K. (2014). Wave activities in separatrix regions of magnetic reconnection. *Geophysical Research Letters*, *41*, 2721–2728. https://doi.org/10.1002/2014GL059893

Fuselier, S. A., Vines, S. K., Burch, J. L., Petrinec, S. M., Trattner, K. J., Cassak, P. A., et al. (2017). Large-scale characteristics of reconnection diffusion regions and associated magnetopause crossings observed by MMS. *Journal of Geophysical Research: Space Physics*, *122*, 5466–5486. https://doi.org/10.1002/2017JA024024

Genestreti, K. J., Burch, J. L., Cassak, P. A., Torbert, R. B., Varsani, A., Ergun, R. E., et al. (2017). The effect of a guide field on local energy conversion during asymmetric magnetic reconnection: MMS observations. *Journal of Geophysical Research: Space Physics*, *122*, 11,342–11,353. https://doi.org/10.1004/2017JA024247

Hesse, M., Aunai, N., Sibeck, D., & Birn, J. (2014). On the electron diffusion region in planar, asymmetric, systems. *Geophysical Research Letters*, *41*, 8673–8680. https://doi.org/10.1002/2014GL061586

Hesse, M., Liu, Y.-H., Chen, L.-J., Bessho, N., Kuznetsova, M., Birn, J., & Burch, J. L. (2016). On the electron diffusion region in asymmetric reconnection with a guide magnetic field. *Geophysical Research Letters*, *43*, 2359–2364. https://doi.org/10.1002/2016GL068373

Hesse, M., Liu, Y.-H., Chen, L.-J., Bessho, N., Wang, S., Burch, J., et al. (2018). The physical foundation of the reconnection electric field. *Physics of Plasmas*. arXiv:1801.01090

Hwang, K.-J., Sibeck, D. G., Choi, E., Chen, L.-J., Ergun, R. E., Khotyaintsev, Y., et al. (2017). Magnetospheric multiscale mission observations of the outer electron diffusion region. *Geophysical Research Letters*, *4*, 2049–2059. https://doi.org/10.1002/2017GL072830

Khotyaintsev, Y. V., Graham, D. B., Norgren, C., Eriksson, E., Li, W., Johlander, A., et al. (2016). Electron jet of asymmetric reconnection. *Geophysical Research Letters*, *43*, 5571–5580. https://doi.org/10.1002/2016GL069064

Khrabrov, A. V., & Sonnerup, B. U. Ö. (1998). Orientation and motion of current layers: Minimization of the Faraday residue. *Geophysical Research Letters*, *25*, 2373–2376. https://doi.org/10.1029/98GL51784

Le, A., Daughton, W., Chen, L.-J., & Egedal, J. (2017). Enhanced electron mixing and heating in 3-D asymmetric reconnection at the Earth's magnetopause. *Geophysical Research Letters*, *44*, 2096–2104. https://doi.org/10.1002/2017GL072522

Le Contel, O., Leroy, P., Roux, A., Coillot, C., Alison, D., Bouabdellah, A., et al. (2016). The search-coil magnetometer for MMS. *Space Science Reviews*, *199*, 257–282. https://doi.org/10.1007/s11214-014-0096-9

Lindqvist, P.-A., Olsson, G., Torbert, R. B., King, B., Granoff, M., Rau, D., et al. (2016). The spin-plane double probe electric field instrument for MMS. *Space Science Reviews*, *199*, 137–165. https://doi.org/10.1007/s11214-014-0116-9

Malakit, K., Shay, M. A., Cassak, P. A., & Ruffolo, D. (2013). New electric field in asymmetric magnetic reconnection. *Physical Review Letters*, *111*, 135001. https://doi.org/10.1103/PhysRevLett.111.135001

Nakamura, T. K. M., Eriksson, S., Hasegawa, H., Zenitani, S., Li, W., Genestreti, K. J., et al. (2017). Mass and energy transfer across the Earth's magnetopause caused by vortex-induced reconnection. *Journal of Geophysical Research: Space Physics*, *122*, 11,505–11,522. https://doi.org/10.1004/2017JA024346

Phan, T. D., Shay, M. A., Haggerty, C. C., Gosling, J. T., Eastwood, J. P., Fujimoto, M., et al. (2016). Ion Larmor radius effects near a reconnection X line at the magnetopause: THEMIS observations and simulation comparison. *Geophysical Research Letters*, *43*, 8844–8852. https://doi.org/10.1002/2016GL070224

Phan, T. D., Eastwood, J. P., Cassak, P. A., Øieroset, M., Gosling, J. T., Gershman, D. J., et al. (2016). MMS observations of electron-scale filamentary currents in the reconnection exhaust and near the X line. *Geophysical Research Letters*, *43*, 6060–6069. https://doi.org/10.1002/2016GL069212

Pollock, C., Moore, T., Jacques, A., Burch, J., Gliese, U., Saito, Y., et al. (2016). Fast plasma investigation for magnetospheric multiscale. *Space Science Reviews*, *199*, 331–406. https://doi.org/10.1007/s11214-016-0245-4

Price, L., Swisdak, M., Drake, J. F., Burch, J. L., Cassak, P. A., & Ergun, R. E. (2017). Turbulence in three-dimensional simulations of magnetopause reconnection. *Journal of Geophysical Research: Space Physics*, *122*, 11,086–11,099. https://doi.org/10.1002/2017JA024227

Price, L., Swisdak, M., Drake, J. F., Cassak, P. A., Dahlin, J. T., & Ergun, R. E. (2016). The effects of turbulence on three-dimensional magnetic reconnection at the magnetopause. *Geophysical Research Letters*, *43*, 6020–6027. https://doi.org/10.1002/2016GL069578

Rager, A. C., Dorelli, J. C., Gershman, D. J., Uritsky, V., Avanov, L. A., Torbert, R. B., et al. (2018). Electron crescent distributions as a manifestation of diamagnetic drift in an electron-scale current sheet: Magnetospheric Multiscale observations using new 7.5 ms Fast Plasma Investigation moments. *Geophysical Research Letters*, *45*, 578–584. https://doi.org/10.1002/2017GL076260

Roytershteyn, V., Daughton, W., Karimabadi, H., & Mozer, F. S. (2012). Influence of the lower-hybrid drift instability on magnetic reconnection in asymmetric configurations. *Physical Review Letters*, *108*(18), 185001. https://doi.org/10.1103/PhysRevLett.108.185001

Russell, C. T., Anderson, B. J., Baumjohann, W., Bromund, K. R., Dearborn, D., Fischer, D., et al. (2016). The magnetospheric multiscale magnetometers. *Space Science Reviews*, *199*, 189–256. https://doi.org/10.1007/s11214-014-0057-3

Schwartz, S. J. (1998). Shock and discontinuity normals, Mach numbers, and related parameters. In G. Paschmann & P. W. Daly (Eds.), *Analysis methods for multi-spacecraft data* (chap. 10, pp. 249–270). Bern, Switzerland: International Space Science Institute.

Shay, M. A., Haggerty, C. C., Phan, T. D., Drake, J. F., Cassak, P. A., Wu, P., et al. (2014). Electron heating during magnetic reconnection: A simulation scaling study. *Physics of Plasmas*, *21*(12), 122902. https://doi.org/10.1063/1.4904203

Shay, M. A., Phan, T. D., Haggerty, C. C., Fujimoto, M., Drake, J. F., Malakit, K., et al. (2016). Kinetic signatures of the region surrounding the X line in asymmetric (magnetopause) reconnection. *Geophysical Research Letters*, *43*, 4145–4154. https://doi.org/10.1002/2016GL069034

Shue, J.-H., Song, P., Russell, C. T., Steinberg, J. T., Chao, J. K., Zastenker, G., et al. (1998). Magnetopause location under extreme solar wind conditions. *Journal of Geophysical Research*, *103*(A8), 17,691–17,700. https://doi.org/10.1029/98JA01103

Swisdak, M. (2016). Quantifying gyrotropy in magnetic reconnection. *Geophysical Research Letters*, *43*, 43–49. https://doi.org/10.1002/2015GL066980

Torbert, R. B., Burch, J. L., Giles, B. L., Gershman, D., Pollock, C. J., Dorelli, J., et al. (2016). Estimates of terms in Ohm's law during an encounter with an electron diffusion region. *Geophysical Research Letters*, *43*, 5918–5925. https://doi.org/10.1002/2016GL069553

Wang, S., Chen, L.-J., Hesse, M., Wilson, L. B., Bessho, N., Gershman, D. J., et al. (2017). Parallel electron heating in the magnetospheric inflow region. *Geophysical Research Letters*, *44*, 4384–4392. https://doi.org/10.1002/2017GL073404

Wang, R., Nakamura, R., Lu, Q., Baumjohann, W., Ergun, R. E., Burch, J. L., et al. (2017). Electron-scale quadrants of the hall magnetic field observed by the magnetospheric multiscale spacecraft during asymmetric reconnection. *Physical Review Letters*, *118*, 175101. https://doi.org/10.1103/PhysRevLett.118.175101

Zenitani, S., Hesse, M., Klimas, A., & Kuznetsova, M. (2011). New measure of the dissipation region in collisionless magnetic reconnection. *Physical Review Letters*, *106*(19), 195003. https://doi.org/10.1103/PhysRevLett.106.195003